AGU PUBLICATIONS

Radio Science

RESEARCH ARTICLE
10.1002/2015RS005858

Key Points:
- The atmospheric microwave absorption by dry air and water vapor is determined from GPM satellite observations
- An improved model for the water vapor continuum absorption and the 22.235 GHz water vapor line is found
- An improved model for the dry air continuum absorption and nonresonant oxygen absorption is found

Correspondence to:
T. Meissner,
meissner@remss.com

Citation:
Wentz, F. J., and T. Meissner (2016), Atmospheric absorption model for dry air and water vapor at microwave frequencies below 100 GHz derived from spaceborne radiometer observations, *Radio Sci.*, *51*, doi:10.1002/2015RS005858.

Received 13 NOV 2015
Accepted 8 APR 2016
Accepted article online 14 APR 2016

Atmospheric absorption model for dry air and water vapor at microwave frequencies below 100 GHz derived from spaceborne radiometer observations

Frank J. Wentz[1] and Thomas Meissner[1]

[1]Remote Sensing Systems, Santa Rosa, California, USA

Abstract The Liebe and Rosenkranz atmospheric absorption models for dry air and water vapor below 100 GHz are refined based on an analysis of antenna temperature (T_A) measurements taken by the Global Precipitation Measurement Microwave Imager (GMI) in the frequency range 10.7 to 89.0 GHz. The GMI T_A measurements are compared to the T_A predicted by a radiative transfer model (RTM), which incorporates both the atmospheric absorption model and a model for the emission and reflection from a rough-ocean surface. The inputs for the RTM are the geophysical retrievals of wind speed, columnar water vapor, and columnar cloud liquid water obtained from the satellite radiometer WindSat. The Liebe and Rosenkranz absorption models are adjusted to achieve consistency with the RTM. The vapor continuum is decreased by 3% to 10%, depending on vapor. To accomplish this, the foreign-broadening part is increased by 10%, and the self-broadening part is decreased by about 40% at the higher frequencies. In addition, the strength of the water vapor line is increased by 1%, and the shape of the line at low frequencies is modified. The dry air absorption is increased, with the increase being a maximum of 20% at the 89 GHz, the highest frequency considered here. The nonresonant oxygen absorption is increased by about 6%. In addition to the RTM comparisons, our results are supported by a comparison between columnar water vapor retrievals from 12 satellite microwave radiometers and GPS-retrieved water vapor values.

1. Introduction

In the absence of clouds and rain, the absorption and re-emission of microwave radiation propagating through the Earth's atmosphere are governed by the absorption coefficients for dry air, including molecular oxygen and nitrogen, and for water vapor: α_D and α_V. The specification of these two coefficients as functions of radiation frequency f (GHz), air temperature T_a (K), dry air pressure p (kPa), and water vapor pressure e (kPa) has been the subject of investigation since *Becker and Autler* [1946], *Van Vleck* [1947], and *Birnbaum* [1953].

Here we investigate these α_D and α_V functionalities using satellite measurement of the microwave radiation upwelling from the Earth. The most accurate radiative transfer model (RTM) for this Earth radiation is for rain-free observations over the oceans. Furthermore, the ocean surface is radiometrically cold (≈90 K for horizontal polarization at the lower microwave frequencies), and this cold surface provides a high contrast for observing variations in α_D and α_V. For example, a change in α_D or α_V of 0.00005 km^{-1} (0.0002 dB/km) produces a change of about 0.1 K in the ocean brightness temperature (T_B) seen by a microwave radiometer onboard a satellite. The 0.1 K precision is typical of todays' advanced satellite microwave radiometers particularly after averaging over millions of space-based observations [*Wentz and Draper*, 2015]. The sensitivity of 0.00005 km^{-1} is much higher than is generally reported in the extensive literature on α_D and α_V [*Liebe*, 1981, 1985, 1989; *Clough et al.*, 1989; *Liebe et al.*, 1992; *Rosenkranz*, 1998; *Tretyakov et al.*, 2005; *Payne et al.*, 2008, 2011].

Taking advantage of this high sensitivity, we have derived new expressions for α_D and α_V. This derivation is based on satellite T_B observations in the 11 to 89 GHz range. Our primary goal is to improve the atmospheric absorption model so it can be used together with our surface emission model [*Meissner and Wentz*, 2004, 2012] to form a complete and accurate RTM for the ocean surface and intervening atmosphere. This RTM can then be used for analysis and calibration of past, present, and future spaceborne MW sensors. We are not considering sounding channels that operate within the 50–70 GHz band of densely spaced oxygen lines. These oxygen lines are excluded from our analysis, and we only study the continuum parts of α_D. The coefficients α_D and α_V are derived such that the ocean RTM T_B equals satellite measurements of T_B over the full range of water vapor values (i.e., from the tropics to the cold, dry polar regions).

2. Formulation

In the absence of rain, the ocean brightness temperature T_B as seen by an orbiting satellite instrument is given by

$$T_B = T_{BU} + \tau(0,H)\left[ET_s + (1-E)\left(T_{BD} + \tau(0,H)T_{B,\text{space}}\right)\right] + \tau(0,H)T_{B,\text{scat}}$$
$$T_{B,\text{scat}} = \Omega(1-E)\left[T_{BD} + \tau(0,H)T_{B,\text{space}} - T_{B,\text{space}}\right] \quad (1)$$

Here T_{BU} and T_{BD} are the upwelling and downwelling atmospheric brightness temperatures, $T_{B,\text{space}}$ is the temperature of the cosmic microwave background radiation (cold space), $\tau(0,H)$ is the total transmittance through the atmosphere, E and T_s are the emissivity and temperature of the ocean surface, and H is the height at which the atmospheric absorption is effectively zero. For the microwave frequencies considered here, $H = 12$ km. The sea surface emissivity E is a function of wind speed W and wind direction ϕ_w. The term $T_{B.\,\text{scat}}$, which is proportional to the empirical factor Ω term, is a small adjustment that accounts for scattering as opposed to reflections from the sea surface, as discussed by *Wentz and Meissner* [2000] and *Meissner and Wentz* [2012]. The upwelling and downwelling T_B are found by integration through the atmosphere

$$T_{BU} = \sec\theta_i \int_0^H dh\alpha(h)T_a(h)\,\tau(h,H) \quad (2)$$

$$T_{BD} = \sec\theta_i \int_0^H dh\alpha(h)T_a(h)\,\tau(0,h) \quad (3)$$

where θ_i is the angle between the satellite viewing direction and the Earth's geoid and is called the Earth incidence angle, h is the height (km) above the Earth's surface, $\alpha(h)$ is the atmospheric absorption coefficient, $T_a(h)$ is the air temperature, and $\tau(h_1,h_2)$ is the atmospheric transmission function given by

$$\tau(h_1,,h_2) = \exp\left(-\sec\theta_i \int_{h_1}^{h_2} dh\alpha(h)\right) \quad (4)$$

The atmospheric absorption coefficient (km^{-1}) consists of three components: dry air, water vapor, and cloud water.

$$\alpha(h) = \alpha_D(h) + \alpha_V(h) + \alpha_C(h) \quad (5)$$

Wentz [1983, 1997] shows that the integrals in (2), (3), and (4) can be well approximated by analytical expressions that are functions of sea surface temperature T_S, columnar water vapor V, and columnar cloud liquid water C.

$$V = \int_0^H dh\rho_V \quad (6)$$

where ρ_V is water vapor density. A similar expression holds for C.

3. Inputs to RTM

The calculation of T_B requires the following model inputs: T_s, ϕ_w, W, V, and C. T_s comes from the NOAA sea surface temperature (SST) operational product [*Reynolds et al.*, 2002], and ϕ_w comes the National Centers for Environmental Prediction 6 h wind fields. We do not use T_s from WindSat because T_S can only be retrieved over a narrow portion of the WindSat swath that contains the 7 GHz observations. The sensitivity of T_B to ϕ_w is small, and when the data are averaged, any errors in ϕ_w become negligible for the type of analysis we are presenting here. The remaining environmental parameters (W, V, and C) come from the satellite observations via a geophysical retrieval algorithm. For our analysis, the most important of these parameters is V.

We compute the ocean surface emissivity E component of the RTM from T_s, W, and ϕ_w using the dielectric model of *Meissner and Wentz* [2004] and our rough surface emission model [*Meissner and Wentz*, 2004, 2012].

The vapor retrieval algorithm was initially developed using radiosonde observations as the absolute calibration reference [*Wentz*, 1997]. Since then, there have been algorithm updates but the radiosonde absolute calibration has been maintained. For the current algorithm [*Mears et al.*, 2015] the bias of the satellite minus the radiosonde vapor is 0.05 mm using the radiosonde data set described in *Wentz* [1997]. Comparisons have also been done with V derived from the vapor-dependent delay of GPS satellite radio signals [*Mears et al.*, 2015]. Vapor data from nine satellite microwave radiometers spanning 25 years were used in the comparisons. The standard deviations for individual GPS matchups were found to be 2 mm or less. When averaged over many matchups, the systematic error, excluding overall bias, was about 0.5 mm from 0 to 60 mm of vapor. Based on this GPS analysis, we expect the accuracy of the columnar vapor for our analysis to be of a similar accuracy when sufficiently averaged.

The wind algorithm was likewise developed and also has been thoroughly evaluated [*Wentz*, 1997; *Mears et al.*, 2001; *Wentz*, 2015]. In this case, it was ocean buoy wind speeds that are the absolute calibration reference. Comparisons of radiometer wind speeds with moored buoy observations typically show standard deviations near 1 m/s for individual matchups. However, some of this error is due to the spatial/temporal mismatch between the buoy point observation and the much larger field of view of the satellite (20–50 km). Also, the satellite "wind" retrieval is more of a measure of surface roughness than the actual wind speed at 5 to 10 m above the surface. For this analysis, W is only used to find the sea surface emissivity E, and hence, it is to our advantage that W is more of a roughness indicator than a wind speed indicator. Collocation of W from pairs of satellite radiometers typically shows a standard deviation of 0.7 to 0.8 m/s. This suggests that the accuracy of W when interpreted as an indicator of roughness is $0.75/\sqrt{2} = 0.5$ m/s. When averaged over millions of observations, the error related to W is very small.

For the cloud algorithm, we do not have a good absolute calibration reference other than clear skies, for which $C = 0$. The fact that a high percentage of observations is clear skies allows us to use a histogram technique to evaluate the cloud retrieval. An ensemble of cloud histograms are generated for various stratifications of T_s, V, and W. These cloud histograms are all required to have the same alignment for $C = 0$. *Wentz* [1997] used this technique to demonstrate that the self-broadening water vapor continuum absorption α_V of *Liebe* [1985] at 37 GHz was about 20% too high, a problem also detected later by *Payne et al.* [2011]. The evidence for this was that the cloud retrievals from the Special Sensor Microwave Imagers (SSMI) showed an obvious error that was directly related to V. At high water vapor, the cloud retrievals were negative. This was due to the vapor continuum being too large and in turn the vapor correction to the cloud retrieval was too large, resulting in an overcorrection that biased the cloud values low. In addition to the $C = 0$ alignment requirement, the cloud algorithm relies on the Rayleigh scattering approximation to specify α_C and the permittivity of liquid cloud water [*Meissner and Wentz*, 2004].

4. Satellite Versus Model Comparisons

To compare the model brightness temperature (1) to satellite observations, the antenna characteristics of the satellite microwave radiometer must be considered. The model representation of the antenna temperature T_A measured by the radiometer is given by

$$T_{Av,\mathrm{rtm}} = (1-\eta)\frac{T_{Bv} + \chi T_{Bh}}{1+\chi} + \eta T_{B,\mathrm{space}} \tag{7}$$

where we have now introduced polarization notation, with subscripts v and h denoting vertical and horizontal polarization, respectively. Polarization comes into (7) due to the surface emissivity E being polarized. The subscript rtm denotes that this T_A is computed from the radiative transfer model described above. The term η is the antenna spillover, which is the fraction of received power coming from cold space as opposed to coming from Earth. The term χ is the fraction of orthogonally polarized power that is received. $T_{B,\mathrm{space}}$ is near 2.73 K. Its effective value that is used in the computation accounts for the deviation of the Rayleigh-Jeans approximation from the Planck law and depends on frequency [*Meissner et al.*, 2012]. The h-pol T_A is also given by (7), but with the v and h subscripts reversed.

For the satellite T_A measurements, we use those obtained from the microwave radiometer that flies on NASA's Global Precipitation Mission (GPM) Core Observatory [*Hou et al.*, 2014]. The sensor, called GMI for GPM Microwave Imager, is the first satellite microwave imager to employ a dual onboard calibration system. In addition to a mirror viewing cold space and a blackbody hot load, GMI also has noise diodes to provide

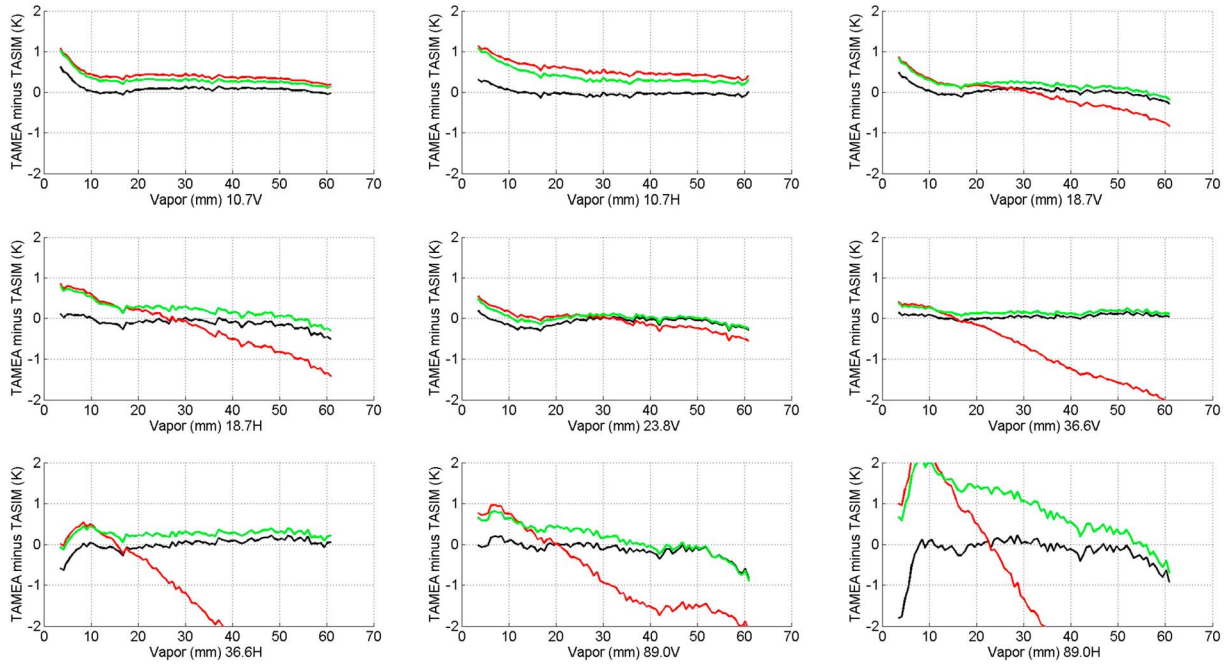

Figure 1. Measured minus RTM computed antenna temperatures for the nine lowest GMI channels: Red curves: using the dry air coefficients given by *Liebe* [1989] and *Liebe et al.* [1992] and the vapor coefficients given by *Rosenkranz* [1998]. Green curves: after adjusting the water vapor absorption. Black curves: after adjusting both water vapor and dry air absorption.

redundant calibration and a direct measurement of the sensor's nonlinearity. Several orbital maneuvers were performed to establish an absolute calibration of T_A near 0.2 K [*Wentz and Draper*, 2015]. GMI has 14 channels ranging from 11 GHz to 183 GHz. Here we only consider the nine lower channels that go up to 89 GHz. The atmospheric absorption for the higher frequencies of 166 GHz and 183 GHz is very large, and the RTM computation is very sensitive to the details of vapor and temperature profiles. The GMI T_A measurements are denoted by $T_{A,\mathrm{gmi}}$. The values for GMI η and χ are given by *Wentz and Draper* [2015].

For this analysis, the first 13 months of GMI observations (March 2014 through March 2015) are used. Since the analysis requires *W*, *V*, and *C* retrievals, we need geophysical retrievals from a second satellite instrument at nearly the same time and location as the GMI T_A observations. For this, we use the geophysical retrievals from the microwave imager WindSat that flies on the Navy's Coriolis satellite. The collocation criterion is that WindSat ocean retrievals are rain free, are within ±1 h of the GMI T_A observation, and are within a spatial collocation window of 25 km.

We consider WindSat to be the best calibrated sensor that is collocated with GMI. The WindSat ocean retrievals have been thoroughly validated by *Wentz* [2015] and many others [*Meissner et al.*, 2011; *Mears et al.*, 2015; *De Biasio and Zecchetto*, 2013; *Huang et al.*, 2014] against buoy measurements, GPS vapor measurements, and geophysical retrievals for other satellites. WindSat has proven to be a very stable sensor. Comparisons of WindSat SST and winds with ocean buoys and WindSat vapor with GPS-derived vapor show no obvious evidence of drift. Comparisons with Tropical Rainfall Measuring Mission Microwave Imager (TMI) also verify the stability of WindSat [*Wentz*, 2015].

5. Adjustments to the Dry Air and Vapor Absorption Coefficients

Our derivation of α_D and α_V is based on an analysis of the measured-minus-modeled T_A differences.

$$\Delta T_A = T_{A,\mathrm{gmi}} - T_{A,\mathrm{rtm}} \tag{8}$$

Figure 1 shows ΔT_A plotted versus columnar water vapor *V*. Each frame corresponds to one of the nine lower frequency GMI channels. The lines in Figure 1 (and Figure 4 below) are generated taking 1 min averages of ΔT_A during the course of a satellite orbit. These 1 min averages are then put in vapor bins that are 0.7 mm

wide. The number of samples in a bin ranges from about 500 to 2000. The values plotted in Figure 1 are the bin averages. The standard deviations of the bin samples range from 0.5 to 1.5 K, except for 89 GHz h-pol, for which it is 2.7 K. The random component of the error, which is reduced by the square root of the number of samples, is less than 0.1 K for all channels.

The red curves in Figure 1 are the results obtained when using the dry air coefficient given by *Liebe* [1989] and *Liebe et al.* [1992] and the vapor coefficient given by *Rosenkranz* [1998]. For the dry air coefficient, the formulation is from *Liebe* [1989] but the numerical values of the parameters in the formulation are taken from *Liebe et al.* [1992]. The most obvious feature in the plot is the strong negative slope of ΔT_A at the higher frequencies. This is due to the same problem mentioned above: the water vapor continuum is too strong at higher frequencies. The unmodified *Rosenkranz* [1998] vapor continuum in terms of km^{-1} is

$$\alpha_{Vc} = 0.41907\times 10^{-1} f^2 \theta^3 \left(a_1 pe + a_2 \theta^{4.5} e^2\right) \tag{9}$$

where the dimensionless term θ is $300/T_a$. The coefficients a_1 (foreign-broadening part) and a_2 (self-broadening part) were derived from best fits to laboratory measurements. The values are 1.296E-6 and 4.295E-5, respectively. We found that the following modification to the a_1 and a_2 coefficients removed the correlation of ΔT_A with V over the frequency range from 19 to 89 GHz

$$\alpha_{Vc}^{'} = 0.41907\times 10^{-1} f^2 \theta^3 \left(1.1 a_1 pe + 0.425 f^{0.1} a_2 \theta^{4.5} e^2\right) \tag{10}$$

where we use the prime sign to indicate the modified coefficient. For typical water vapor values near 25 mm, the modification is about a 3% reduction. At high values near $V = 50$ mm, the reduction is about 10%. This reduction is considerably less than the 20% reduction that was required for the *Liebe* [1985] model in *Wentz* [1997]. Our adjusted water vapor continuum absorption model (10) is in very good agreement with the results of *Payne et al.* [2011]. In addition, the partitioning of foreign- and self-broadening parts agrees well with *Turner et al.* [2009], who obtained adjustment factors of 1.105 and 0.79, respectively, at 150 GHz. If we extrapolate our results above 100 GHz, then our adjustment factors at 150 GHz are 1.10 and 0.70, respectively.

A much smaller adjustment is made to the 22 GHz vapor line shape. Looking at comparisons of satellite water vapor retrievals with radiosondes and vapor values derived from GPS satellites, we conclude that a 1% increase in the strength of the 22 GHz line gives slightly better agreement over the full range of V from 5 to 65 mm.

$$S_{22.235}^{'} = 1.01 S_{22.235} \tag{11}$$

We also find that after applying the adjustments to the dry air absorption, to be discussed below, there was a small residual correlation of ΔT_A with V at 11 GHz. This is corrected by slightly increasing the low-frequency wing of the line. Noting that the Gross line shape [*Gross*, 1955] has more absorption in the low-frequency wing than does the Van Vleck-Weisskopf shape [*Van Vleck and Weisskopf*, 1945], we transform the Van Vleck-Weisskopf shape to the Gross shape at the lower frequencies using the following generalized line shape [*Ben-Reuven,* 1965, 1966]:

$$\phi(f) = \frac{2}{\pi}\frac{f}{f_o}\frac{(\gamma-\chi)f^2 + (\gamma+\chi)\left(f_o^2+\gamma^2-\chi^2\right)}{\left(f^2 - f_o^2 - \gamma^2 + \chi^2\right)^2 + 4f^2\gamma^2} \tag{12}$$

where γ is the line half width, f_o is the center frequency (22.2351 GHz), and χ is an adjustable parameter. For $\chi = 0$, $\phi(f)$ is the Van Vleck-Weisskopf shape and for $\chi = \gamma$, $\phi(f)$ is the Gross shape. The following expression, which is applied for 2.5 GHz $< f <$ 19 GHz, smoothly transforms the Van Vleck-Weisskopf shape to the Gross shape as f goes from 19 to 2.5 GHz.

$$\chi = \gamma x^2 (3 - 2x) \tag{13}$$

$$x = \frac{19 - f}{16.5} \tag{14}$$

The green line in Figure 1 shows ΔT_A after applying the above corrections to the water vapor continuum and 22 GHz line shape. Changing the water vapor absorption has little or no effect for low vapor values. To remove the ΔT_A bias for the low vapor values, we adjust the dry air absorption. Two changes are made to the *Liebe* [1989] formulation. The first is to the width parameter $\gamma_{O,nr}$ for the nonresonant oxygen absorption, which becomes dominant at very low frequencies. The *Liebe* [1989] value is

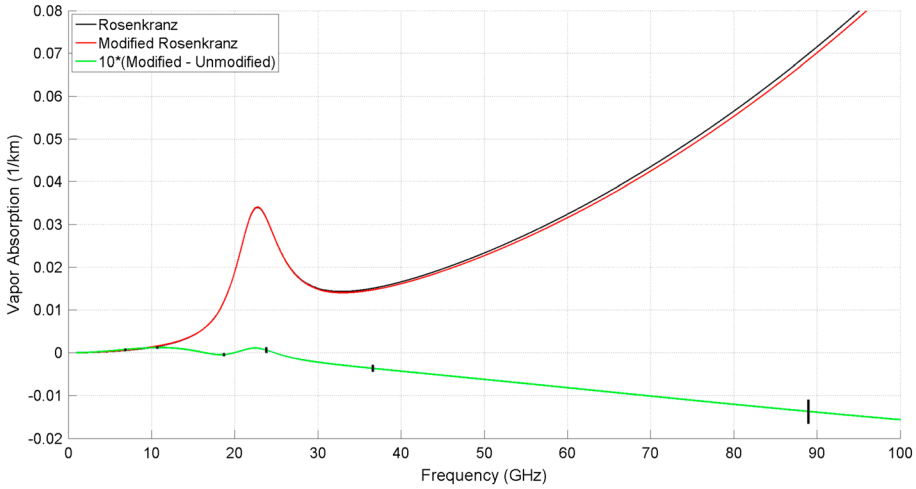

Figure 2. Total water vapor absorption (km^{-1}) from *Rosenkranz* [1998] (black curve) and after making the adjustments in this paper (red curve). The green curve shows 10 times the difference between the adjusted and unadjusted water vapor absorption model. The black vertical lines are error bars, which are also multiplied by 10 to be consistent with the green curve.

$$\gamma_{O,\mathrm{nr}} = 0.0056(p + 1.1e)\theta \tag{15}$$

We modified this expression by increasing the θ exponent to 1.5.

$$\gamma'_{O,\mathrm{nr}} = 0.0056(p + 1.1e)\theta^{1.5} \tag{16}$$

This increases the dry air absorption by about 5–7% depending on T_a, with the increase being essentially independent of frequency for $f > 2$ GHz. The 0.0056 coefficient could have been increased instead with similar results. However, changing the exponent had the benefit of producing somewhat more absorption for low water vapors, for which T_a is colder, and this slightly mitigated the upturn in the 10.7 GHz ΔT_A observed at low water vapors as shown in Figure 1.

The second change is to the pressure-induced nitrogen absorption continuum. It is part of the dry air absorption and becomes noticeable for the higher frequencies. Therefore, it needs to be added to the oxygen line absorption and the nonresonant oxygen continuum absorption. The *Liebe* [1989] expression in terms of km^{-1} is

$$\alpha_{Dc} = 0.58670\times10^{-11} f^2 p^2 \theta^{3.5}\left(1 - 1.2\times10^{-5} f^{1.5}\right) \tag{17}$$

To this we add an additional dry air absorption for frequencies above 37 GHz

$$\alpha'_{Dc} = \alpha_{Dc} + 0.10896\times10^{-9} p^2 \theta^3 (f - 37)^{1.8}\, u(f - 37) \tag{18}$$

where $u(x)$ is the unit step function. We use a temperature exponent of 3, which is the same as what *Liebe* [1989] used for the strength of the oxygen lines.

Oxygen and nitrogen are uniformly mixed in the atmosphere, so there is no way to distinguish solely from atmospheric measurements which one, or both, should be modified. Our choice is to minimize changes to Liebe's model, and hence, we increase his nitrogen absorption term. However, physical mechanism actually responsible for this increase could well be O_2-O_2 and O_2-N_2 collisions [*Boissoles et al.*, 2003]

The black lines in Figure 1 show ΔT_A after we apply both the water vapor and the dry air adjustments. Comparing the green and black curves shows that modifying $\gamma_{O,\mathrm{nr}}$ removes nearly all of the remaining ΔT_A biases for frequencies up to 37 GHz. Above 37 GHz, modification (18) is required to remove ΔT_A biases at low water vapors. With all adjustments applied, ΔT_A is generally within a ±0.2 K envelope, except for some channels at very low and high vapor values. The 11 V and 19 V ΔT_A both show an upturn for $V = 5$ mm. These channels are sensitive to T_S, and the upturn may be due to an error in the Reynolds T_s in cold water.

We also want to note that the bias that is observed in ΔT_A without the adjustments (red curve in Figure 1) is roughly twice as large for horizontal polarization as for vertical polarization. This relationship suggests that

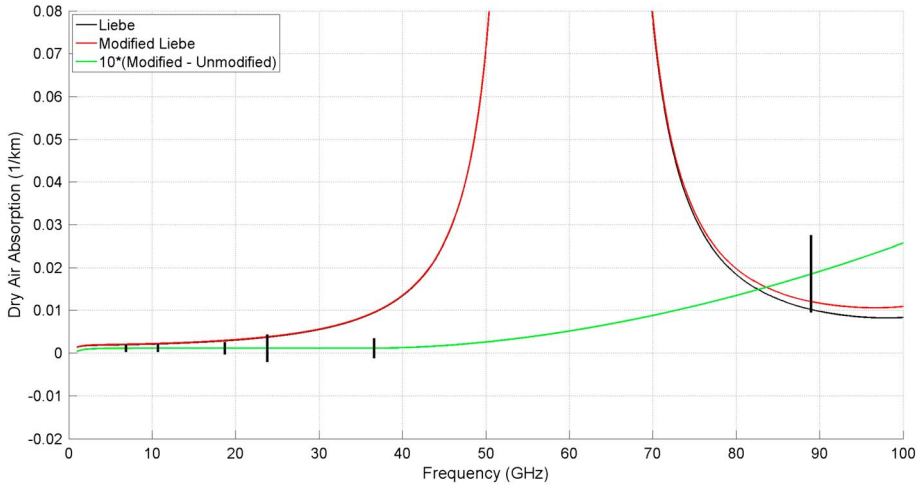

Figure 3. Total dry air absorption (km^{-1}) from *Liebe et al.* [1992] (black curve) and after making the adjustments in this paper (red curve). The green curve shows 10 times the difference between the adjusted and unadjusted dry air absorption model. The black vertical lines are error bars, which are also multiplied by 10 to be consistent with the green curve.

we are dealing with an uncertainty in the atmospheric model rather than an uncertainty in the seawater permittivity model that is used in computing the surface emissivity. For the GMI frequencies and Earth incidence angles, the h-pol reflectivity is about twice as large as the v-pol reflectivity, and therefore, according to the RTM equation (1), an error in the atmospheric absorption impacts the h-pol T_B twice as much as the v-pol T_B [*Meissner and Wentz*, 2002, 2012]. If the error was in the water permittivity model it would impact the v-pol more than the h-pol [*Meissner and Wentz*, 2004].

Figure 2 shows α_V and α'_V for typical midlatitude values of $T_a = 275$ K, $p = 100$ kPa, and $e = 8$ kPa. The figure shows that the change to the shape of the Van Vleck-Weisskopf vapor line is very small, and we hesitate to conclude too much. Possibly, our results are closer to the true line shape, or possibly our modifications are compensating for other effects not fully understood. Figure 3 shows α_D and α'_D, again for typical midlatitude values of T_a, p, and e. Below 37 GHz the small increase in α'_D is due to modifying $\gamma_{O,\mathrm{nr}}$, and this change is nearly independent of frequency. Above 37 GHz, modification (18) takes effect and one sees a significant increase in α'_D relative to α_D.

The results reported here are in good agreement with those found from earlier, unpublished analyses of the SSMI, AMSR, and WindSat satellite sensors. With respect to modifications (11), (13), and (16), the GMI observations supported the modifications found previously, and there was no reason to make a change. The GMI-derived modifications (10) and (18), which relate to the vapor and pressure-induced nitrogen continuum, are slightly different than found from the earlier analyses. For the most part, the GMI results indicate that the prior adjustments were a bit too much. For the vapor continuum adjustment (10), we had previously used $0.375\ f^{0.15}$ rather than $0.425\ f^{0.1}$ for the modification to the self-broadening a_2 term. At 89 GHz, the GMI-derived adjustment is 10% less than the previous adjustment. The prior adjustment that was added to the pressure-induced nitrogen absorption was

$$\alpha''_{Dc} = \alpha_{Dc} + 0.125721\times10^{-10} f^2 p^2 \theta^3 \tag{19}$$

where the double prime indicates prior adjustment. For the GMI-derived modification (18), no adjustment is needed for frequencies at 37 GHz and below. At 89 GHz, the GMI modification (18) increases α_{Dc} by about 17%, while the prior modification (19) gave a 13% increase.

6. Comparison of Satellite Vapor Retrievals With GPS Vapors

In addition to requiring ΔT_A be near zero over the full range of V, as is shown in Figure 1, the other requirement is that the satellite vapor retrievals be consistent with the GPS vapors. *Mears et al.* [2015] show that this is the case, and Table 1 summarizes the *Mears et al.* [2015] results in term of the slope

Table 1. Slope S_{vap} (Percentage) for Satellite Versus GPS Vapor Comparisons

F10	F11	F13	F14	F15	F16	F17	AMSR-E	AMSR2	WindSat	TMI	GMI
−0.55	0.03	−0.08	0.23	0.10	−0.14	−0.04	0.91	−0.14	0.16	0.95	−0.30

$$S_{vap} = \frac{V_{sat} - V_{gps}}{\frac{1}{2}\left(V_{sat} + V_{gps}\right)} \tag{20}$$

where V_{sat} and V_{gps} are the satellite vapor retrieval and the GPS vapor retrieval. Results are shown for 12 satellite sensors. The slope S_{vap} is found by finding collocated pairs of V_{sat} and V_{gps} and binning the difference according to the average. A least squares slope S_{vap} is then found for all bins from 0 to 60 mm. S_{vap} does not exceed 1%. Above 60 mm, all sensors, except Advanced Microwave Scanning Radiometer–EOS (AMSR-E), show V_{sat} biased low relative to V_{gps} by about 0.5 mm. There is little data above 60 mm, and we are not sure what this bias may be due to.

Liljegren et al. [2005] reported that a decrease of 5% in the *Rosenkranz* [1998] air-broadened half-width γ_{dry} for the 22 GHz vapor line greatly improved the agreement between the Rosenkranz model and brightness temperatures obtained from upward looking radiometers during the February 2000 Atmospheric Radiation Measurement experiment at its Southern Great Plains site. This is a much larger modification than reported here. Figure 4 shows the GMI ΔT_A comparisons when γ_{dry} is decreased by 5%. Significant correlations between ΔT_A versus V occur. At 37 GHz, the ΔT_A versus V correlation could be removed by using a slightly different vapor continuum. However, the real problem is at 19 and 24 GHz, for which the correlations have different signs.

The 5% decrease in γ_{dry} would have its most significant effect on the SSMI and SSMIS vapor retrievals. These two sensor types operate at a frequency 22.235 GHz, which is at the center of the vapor line. At the center frequency, decreasing the γ_{dry} increases the water vapor absorption by 4% (not 5% because of the continuum contribution). The larger absorption translates into a 4% reduction in the V retrievals. Relative to the V retrievals we get with the above model, the reduction is only 3% because our model also increases the 22.235 GHz absorption, but only by 1% rather than 5%. A 3% reduction in V retrievals would be inconsistent with the GPS comparisons shown in Table 1.

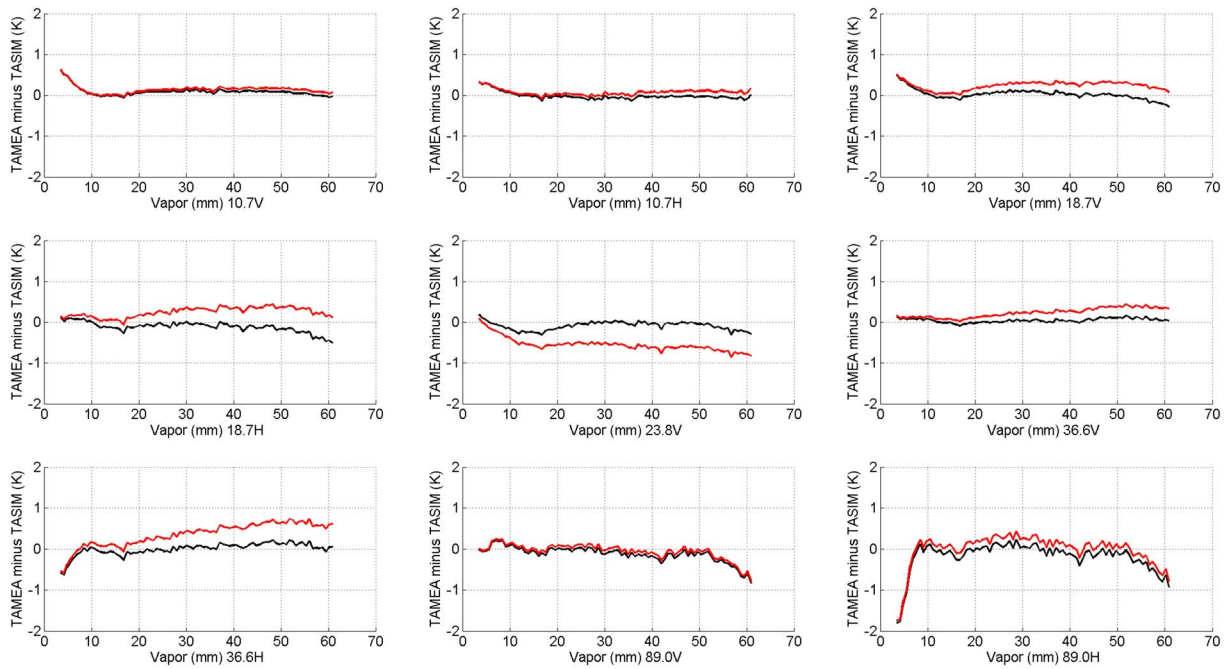

Figure 4. Differences between measured and RTM computed antenna temperatures for the nine lowest GMI channels. The black curves show the results for the absorption model in this paper (same as in Figure 1). The red curves show the results if the air-broadened half-width for the 22 GHz vapor line is decreased by 5% as suggested in *Liljegren et al.* [2005].

7. Uncertainty Analysis

To determine the uncertainty in our derived values for the vapor and dry air absorptions, we use a perturbation analysis. Biases are added to each of the four input parameters (T_s, W, V, and C), to the T_A model and to the v-pol and h-pol T_A measurements. This makes seven perturbation cases. For each case, we find the change in the vapor and dry air absorptions, $\Delta\alpha_D$ and $\Delta\alpha_V$, that restores, as close as possible, the agreement between measurement and the model. To be specific, we find $\Delta\alpha_V$ and $\Delta\alpha_D$ that minimized the following

$$\chi^2 = \left\langle \left(T_{Av,\mathrm{gmi}} - T'_{Av,\mathrm{rtm}}\right)^2 + \left(T_{Ah,\mathrm{gmi}} - T'_{Ah,\mathrm{rtm}}\right)^2 \right\rangle \tag{21}$$

where the prime indicated the RTM T_A with a perturbed input. The angular brackets represent an average over an ensemble of scenes covering the full range of SST, wind, vapor, and cloud occurring for the rain-free oceans. For the perturbation cases that have biases added to the model T_A or the measurement T_A, the cost function is

$$\chi^2 = \left\langle \left(T_{Av,\mathrm{gmi}} - T_{Av,\mathrm{rtm}} + b_v\right)^2 + \left(T_{Ah,\mathrm{gmi}} - T_{Ah,\mathrm{rtm}} + b_h\right)^2 \right\rangle \tag{22}$$

where b_v and b_h are the v-pol and h-pol T_A biases. The dry air change $\Delta\alpha_D$ is modeled as a simple additive offset to α_D. The vapor change $\Delta\alpha_V$ is modeled as

$$\Delta\alpha_V = \beta V \tag{23}$$

where β is the parameter that is found to minimize (21) and (22). The model adjustments $\Delta\alpha_V$ and $\Delta\alpha_D$ for the seven cases are then summed in the root-sum-squared (RSS) sense to obtain a total uncertainty.

The uncertainties that are assigned to each input parameter represent the biases that persist after averaging global for the 13 months used for this study. The uncertainty assigned to T_s is 0.3 C, which is based on comparisons of the Reynolds SST with buoys averaged monthly [*Reynolds and Chelton*, 2010]. The uncertainty assigned to W is 0.3 m/s, which is based on comparisons of wind retrievals from Tropical Rainfall Measuring Mission Microwave Imager (TMI) with buoys [*Wentz*, 2015]. The WindSat wind retrievals have the same, or slightly better, accuracy as TMI. As discussed above, the water vapor retrievals were calibrated to radiosonde observations, and when compared to GPS retrievals, there is a bias of 0.5 mm. This bias could be due to the GPS processing, but this is not clear. For the uncertainty in V we use 0.5 mm, which is in effect assuming that all the bias is in the satellite vapor retrieval, which is worst case. The uncertainty for C is based on the *Wentz and Draper* [2016] global maps of 89 GHz ΔT_A. The sensitivity to C is greatest at 89 GHz. The 89 GHz ΔT_A maps showed systematic features at the ± 0.5 K level that were attributed to mismodeling of clouds. That translates to a ±0.005 mm error in C. Although this error tends to zero when averaged global, we use 0.005 mm as the overall bias in C as worst case.

Errors in the emissivity model are accounted for by assuming 0.25 K and 0.15 K errors in the model's v-pol and h-pol T_A, respectively [*Meissner and Wentz*, 2012]. Errors in the dielectric constant affect v-pol 50% more than h-pol. The polarization signature of the atmospheric model is quite different: v-pol changes are about half the h-pol changes. Because of the different polarization signatures of the atmosphere and surface emissivity, the primary effect of emissivity errors is to produce T_A biases between the model and measurements. Adjustments to the atmosphere cannot remove these v-pol/h-pol biases. Using larger emissivity error values produce unreasonably large T_A biases relative to the GMI observations.

For the last two perturbation cases, offsets are added to the v-pol and h-pol T_A measurements. The absolute accuracy of the GMI T_A measurement is about 0.1 K, and the uncertainty in the specification of the spillover η in (7) adds an additional 0.15 K [*Wentz and Draper*, 2015]. Thus, the total uncertainty assigned to the GMI measurements is 0.25 K for both v-pol and h-pol.

The total (RSS) $\Delta\alpha_V$ and $\Delta\alpha_D$ are shown as error bars in Figures 2 and 3, respectively. Error bars are found for each of the GMI channels and an additional calculation of uncertainty is done at 6.9 GHz. The error bars are overlaid onto the green curve that shows the adjustment applied to the original models. By displaying the error bars in this way, one can better assess the significance of the α_V and α_D adjustments. At the low frequencies below 20 GHz, the $\Delta\alpha_D$ error bars are small and show that the adjustment to the nonresonant oxygen absorption is significant, the sense that the adjustment is larger than the error bar. Likewise at 89 GHz, the adjustment to the nitrogen absorption continuum is significant. The $\Delta\alpha_V$ error bars are smaller than $\Delta\alpha_D$.

8. Conclusions

Liebe [1989] and *Liebe et al.*'s [1992] dry air absorption coefficients and *Rosenkranz*'s [1998] vapor absorption coefficients require only a modest adjustment to obtain consistency with satellite observations of the upwelling microwave radiation coming from the Earth's atmosphere overlying the oceans. The water vapor continuum is reduced by 3% to 10%, depending on vapor. To accomplish this, significant changes are made to the two components making up the continuum: the foreign and self-broadening parts. The foreign-broadening part is increased by 10%, and the self-broadening is decreased by 40% at the higher frequencies. The increase in the nitrogen absorption is a maximum of 20% at the 89 GHz. Minor adjustments are made to the 22.235 GHz line shape and the nonresonant oxygen absorption. With these adjustments, the agreement between the satellite observations and the model is generally at the ±0.2 K level, except for some channels at very low and very high vapor values.

The absorption values found by this investigation are for five distinct frequencies: 10.7, 18.7, 23.8, 36.6, and 89 GHz. We used the modified Liebe and Rosenkranz models to interpolate between these frequencies. Our expectation is that within this range of frequencies, the interpolated model will perform well, having about the same accuracy as at the discrete frequencies. At frequencies below 10.7 GHz, the vapor absorption becomes extremely small and is negligible for most applications. At these low frequencies, the nonresonant oxygen absorption completely dominates, and this term is essentially independent of frequency above 2 GHz. Below 2 GHz, the oxygen absorption tends to zero. Our main concern is extrapolating the results of this study to frequencies above 89 GHz, particularly the dry air and vapor continuum. More investigation is needed at these high frequencies. However, on an encouraging note, when the water vapor continuum derived herein is extrapolated to 150 GHz, it is in very good agreement with the *Turner et al.* [2009] 150 GHz measurements, which were not used in this study.

Acknowledgments
This work has been supported by NASA's Earth Science Division. We are grateful to Carl Mears, Remote Sensing Systems, for providing the analysis comparing the satellite vapor retrievals with the GPS vapor. The L1A GMI antenna temperatures are available from NASA's Precipitation Processing System PPS http://pps.gsfc.nasa.gov/. The values for the WindSat wind speed, columnar water vapor, and columnar cloud liquid water are from Remote Sensing Systems [*Wentz et al.*, 2013]. The NOAA SST operational product is available from ftp://eclipse.ncdc.noaa.gov/pub/OI-daily-v2/IEEE/YYYY/AVHRR-AMSR, where YYYY is the year 2014 to present.

References

Becker, G. E., and S. H. Autler (1946), Water vapor absorption of electromagnetic radiation in the centimeter wave-length range, *Phys.Rev.*, *70*, 300–307.
Ben-Reuven, A. (1965), Transition from resonant to nonresonant line shape in microwave absorption, *Phys. Rev. Lett.*, *14*, 349–351.
Ben-Reuven, A. (1966), Impact broadening of microwave spectra, *Phys. Rev. Lett.*, *145*, 7–22.
Birnbaum, G. (1953), Millimeter wavelength dispersion of water vapor, *J. Chem. Phys.*, *21*(1), 57–61.
Boissoles, J., C. Boulet, R. H. Tipping, A. Brown, and Q. Ma (2003), *J. Quant. Spectros. Radiat. Transfer*, *82*(1–4), 505–516.
Clough, S. A., F. X. Kneizys, and R. W. Davies (1989), Line shape and the water vapor continuum, *Atmos. Res.*, *23*, 229–241.
De Biasio, F., and S. Zecchetto (2013), Comparison of sea surface winds derived from active and passive microwave instruments on the Mediterranean Sea Presentation EGU2013-10157 at the EGU General Assembly Conference, European Geosciences Union, Vienna, Austria.
Gross, E. P. (1955), Shape of collision broadened spectral lines, *Phys. Rev.*, *97*, 395–403.
Hou, A. Y., R. K. Kakar, S. Neeck, A. A. Azarbarzin, C. D. Kummerow, M. Kojima, R. Oki, K. Nakamura, and T. Iguchi (2014), The Global Precipitation Measurement Mission, *Bull. Am. Meteorol. Soc.*, *95*, 701–722.
Huang, X., J. Zhu, M. Lin, Y. Zhao, H. Wang, C. Chen, H. Peng, and Y. Zhang (2014), A preliminary assessment of the sea surface wind speed production of HY-2 scanning microwave radiometer, *Acta Oceanol. Sin.*, *33*, 114–119.
Liebe, H. (1981), Modeling attenuation and phase of radio waves in air at frequencies below 1000 GHz, *Radio Sci.*, *16*(6), 1183–1199, doi:10.1029/RS016i006p01183.
Liebe, H. J. (1985), An updated model for millimeter wave propagation in moist air, *Radio Sci.*, *20*, 1069–1089, doi:10.1029/RS020i005p01069.
Liebe, H. J. (1989), MPM—An atmospheric millimeter-wave propagation model, *Int.J. Infrared Millimeter Waves*, *10*(6), 631–650.
Liebe, H. J., P. W. Rosenkranz, and G. A. Hufford (1992), Atmospheric 60-GHz oxygen spectrum: New laboratory measurements and line parameters, *J. Quant. Spectrosc. Radiat. Transfer*, *48*, 629–643.
Liljegren, J. C., S. A. Boukabara, K. Cady-Pereira, and S. A. Clough (2005), The effect of the half-width of the 22-GHz water vapor line on retrievals of temperature and water vapor profiles with a 12-channel microwave radiometer, *IEEE Trans. Geosci. Remote Sens.*, *43*(5), 1102–1108.
Mears, C. A., D. K. Smith, and F. J. Wentz (2001), Comparison of Special Sensor Microwave Imager and buoy-measured wind speeds from 1987–1997, *J. Geophys. Res.*, *106*, 11,719–11,729, doi:10.1029/1999JC000097.
Mears, C. A., J. Wang, D. K. Smith, and F. J. Wentz (2015), Intercomparison of total precipitable water measurements made by satellite-borne microwave radiometers and ground-based GPS instruments, *J. Geophys. Res. Atmos.*, *120*, 2492–2504, doi:10.1002/2014JD022694.
Meissner, T., and F. J. Wentz (2002), An updated analysis of the ocean surface wind direction signal in passive microwave brightness temperatures, *IEEE Trans. Geosci. Remote Sens.*, *40*(6), 1230–1240.
Meissner, T., and F. J. Wentz (2004), The complex dielectric constant of pure and sea water from microwave satellite observations, *IEEE Trans. Geosci. Remote Sens.*, *42*(9), 1836–1849.
Meissner, T., and F. J. Wentz (2012), The emissivity of the ocean surface between 6–90 GHz over a large range of wind speeds and Earth incidence angles, *IEEE Trans. Geosci. Remote Sens.*, *50*(8), 3004–3026.
Meissner, T., L. Ricciardulli, and F. J. Wentz (2011), All-weather wind vector measurements from intercalibrated active and passive microwave satellite sensors, in *IEEE International Geoscience and Remote Sensing Symposium (IGARSS)*, pp. 1509–1511, IEEE, Vancouver, B. C., and Canada, doi:10.1109/IGARSS.2011.6049354.
Meissner, T., F. J. Wentz, and D. Draper (2012), GMI calibration algorithm and Analysis Theoretical Basis Document (ATBD) Version G, Rep. number 041912, Remote Sensing Systems, Santa Rosa, Calif. [Available at http://www.remss.com/support/publications.]

Payne, V. H., J. S. Delamere, K. E. Cady-Pereira, R. R. Gamache, J. Moncet, E. J. Mlawer, and S. A. Clough (2008), Air-broadened half-widths of the 22- and 183-GHz water-vapor lines, *IEEE Trans. Geosci. Remote Sens.*, *46*(11), 3601–3617.

Payne, V. H., E. J. Mlawer, K. E. Cady-Pereira, and J. Moncet (2011), Water vapor continuum absorption in the microwave, *IEEE Trans. Geosci. Remote Sens.*, *49*(6), 2194–2208.

Reynolds, R. W., and D. B. Chelton (2010), Comparisons of daily sea surface temperature analyses for 2007–08, *J. Clim.*, *23*, 3545–3562, doi:10.1175/2010JCLI3294.1.

Reynolds, R. W., N. A. Rayner, T. M. Smith, D. C. Stokes, and W. Wang (2002), An improved in situ and satellite SST analysis for climate, *J. Clim.*, *15*, 1609–1625.

Rosenkranz, P. (1998), Water vapor microwave continuum absorption: A comparison of measurements and models, *Radio Sci.*, *33*, 919–928, doi:10.1029/98RS01182.

Tretyakov, M. Y., M. A. Koshelev, V. V. Dorovskikh, D. S. Makarov, and P. W. Rosenkranz (2005), 60-GHz oxygen band: Precise broadening and central frequencies of fine-structure lines, absolute absorption profile at atmospheric pressure, and revision of mixing-coefficients, *J. Mol. Spectrosc.*, *231*(1), 1–14.

Turner, D. D., M. P. Cadeddu, U. Löhnert, S. Crewell, and A. M. Vogelmann (2009), Modifications to the water vapor continuum in the microwave suggested by ground-based 150-GHz observations, *IEEE Trans. Geosci. Remote Sens.*, *47*, 3326–3337.

Van Vleck, J. H. (1947), The absorption of microwaves by oxygen and uncondensed water vapor, *Phys. Rev.*, *71*(7), 413–433.

Van Vleck, J. H., and V. F. Weisskopf (1945), On the shape of collision-broadened lines, *Rev. Mod. Phys.*, *17*, 227–236.

Wentz, F. J. (1983), A Model Function for Ocean Microwave Brightness Temperatures, *J. Geophys. Res.*, *88*(C3), 1892–1908, doi:10.1029/JC088iC03p01892.

Wentz, F. J. (1997), A well calibrated ocean algorithm for special sensor microwave/imager, *J. Geophys. Res.*, *102*, 8703–8718, doi:10.1029/96JC01751.

Wentz, F. J. (2015), A 17-year climate record of environmental parameters derived from the Tropical Rainfall Measuring Mission (TRMM) Microwave Imager, *J. Clim.*, *28*, 6882–6902.

Wentz, F. J., and D. Draper (2015), *On-Orbit Absolute Calibration of the Global Precipitation Mission Microwave Imager*, Remote Sensing Systems, Santa Rosa, Calif. [Available at http://images.remss.com/papers/rsspubs/Wentz_JTech_2016_GMI_calibration.pdf.]

Wentz, F. J., and T. Meissner (2000), AMSR Ocean Algorithm Theoretical Basis Document (Version 2), RSS Tech. Proposal 121599A-1, Remote Sensing Systems, Santa Rosa, Calif., December 1999, revised 2000, 66 pp. [Available at http://www.remss.com/support/publications.]

Wentz, F. J., L. Ricciardulli, C. Gentemann, T. Meissner, K. A. Hilburn, and J. Scott (2013), Remote Sensing Systems Coriolis WindSat Environmental Suite. Daily on 0.25 deg grid, Version 7.0.1, Remote Sensing Systems, Santa Rosa, Calif. Accessed 2014 – present. [Available online at www.remss.com/missions/windsat.]